NANO LETTERS

pubs.acs.org/NanoLett

Letter

Dielectric Metasurface for Synchronously Spiral Phase Contrast and Bright-Field Imaging

Yanzeng Zhang, Peicheng Lin, Pengcheng Huo, Mingze Liu, Yongze Ren, Song Zhang, Qianwei Zhou, Yilin Wang, Yan-qing Lu, and Ting Xu*

Cite This: *Nano Lett.* 2023, 23, 2991−2997

Read Online

ACCESS | Metrics & More | Article Recommendations | Supporting Information

ABSTRACT: Spiral phase contrast imaging and bright-field imaging are two widely used modes in microscopy, providing distinct morphological information about objects. However, conventional microscopes are always unable to operate with these two modes at the same time and need additional optical elements to switch between them. Here, we present a microscopy setup that incorporates a dielectric metasurface capable of achieving spiral phase contrast imaging and bright-field imaging synchronously. The metasurface not only can focus the light for diffraction-limited imaging but also can perform a two-dimensional spatial differentiation operation by imparting an orbital angular momentum to the incident light field. This allows two spatially separated images to be simultaneously obtained, one containing high-frequency edge information and the other showing the entirety of the object. Combined with the advantages of planar architecture and ultrathin thickness of the metasurface, this approach is expected to provide support in the fields of microscopy, biomedicine, and materials science.

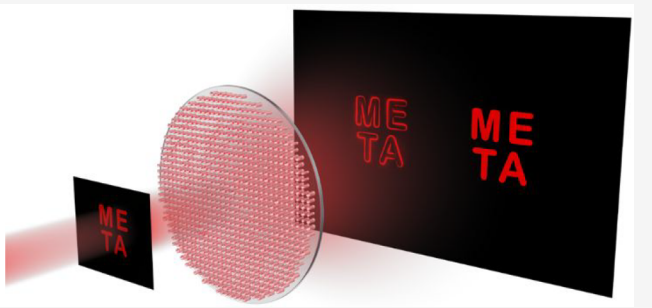

KEYWORDS: *metasurface, orbital angular momentum, phase contrast imaging, edge detection*

Bright-field imaging has always been the preferred imaging mode for observing the entire morphology of light-absorbing objects (i.e., amplitude objects). However, for highly transparent objects (i.e., phase objects), such as unstained biological samples that typically lack substantial amounts of natural pigments, bright-field imaging is unable to clearly distinguish their morphological information. Although staining can be used for high-contrast imaging of transparent biological specimens, it disrupts cell physiology and reduces cell viability.[1] In this context, various phase contrast techniques, such as Zernike phase contrast imaging, differential interference contrast imaging, and spiral phase contrast imaging, have been proposed and demonstrated.[2−6] By extracting the phase information, they can highlight the edges of objects without staining and then conduct living observation of transparent biological specimens.[7−9] Therefore, the combination of bright-field imaging and spiral phase contrast imaging in one microscopy setup would significantly extend the application scenarios.

Most of the current microscopes rely on a serial of optical elements, such as a liquid-crystal-based phase plate and spatial light modulator, to mechanically switch between different imaging modes, which offers a multifunctional imaging capability at the expense of large volume, limited resolution, and high cost.[7,10−15] Furthermore, in certain biomedical imaging applications, such as observing transparent live cells migrating in complex environments, both amplitude and phase objects are present. To capture real-time overall information in such scenarios, developing a compact microscope with the ability of synchronous spiral phase contrast imaging and bright-field imaging in the same field of view is crucial.

In recent years, a metasurface, a flat optical element incorporating nanostructures, breaks through the limitations of conventional optical elements with its advantage of excellent light field control capability, subwavelength pixel resolution, and ultrathin thickness.[16,17] The free control of phase, amplitude, frequency, and polarization enables simultaneous superposition of multidimensional information on a single metasurface.[18−26] Based on the metasurface, a number of novel photonic devices, such as metalens, metaholograms, nanostructural colors, microspectrometers, and metaprocessors have been demonstrated.[27−39] Specially, a photonic spin-multiplexing metasurface has been proposed and used for switchable spiral phase contrast imaging.[40] By designing the polarization-dependent phase profiles and placing the metasurface at the

Received: January 31, 2023
Revised: March 23, 2023
Published: March 27, 2023

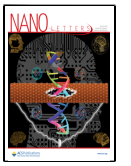

https://doi.org/10.1021/acs.nanolett.3c00388
Nano Lett. 2023, 23, 2991−2997

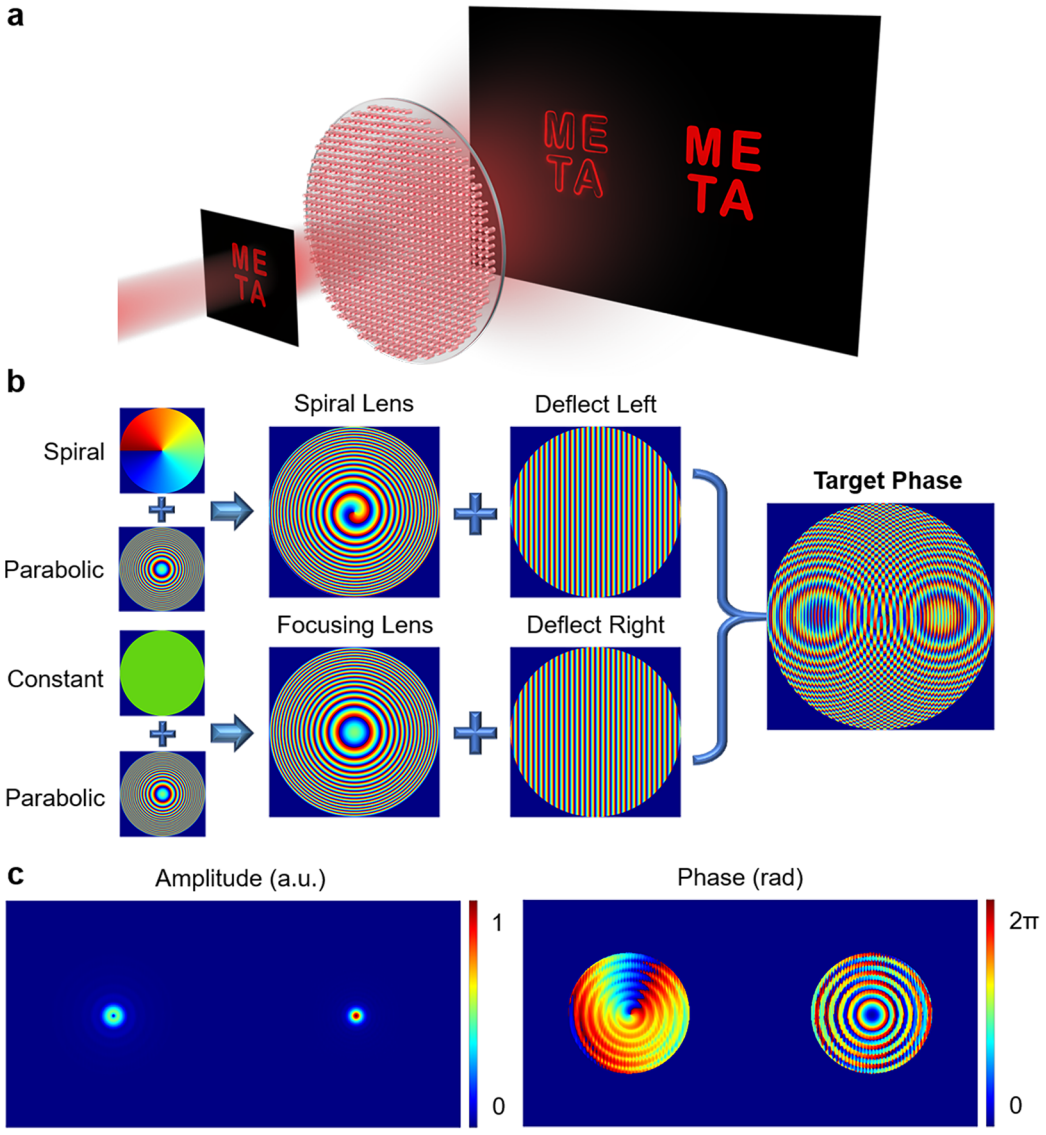

Figure 1. (a) Schematic illustration of the imaging principle based on the proposed dielectric metasurface. After the object light field is modulated by the metasurface, a bright-field image containing the entire information on the object and another spiral phase contrast image with edge information appear simultaneously at the image plane. (b) Phase design principle and distribution of the metasurface. The target phase is composed of two parts; one is the superposition of spiral phase, parabolic focusing phase, and deflection phase, and the other is the combination of constant phase, parabolic focusing phase, and reverse deflection phase. (c) Amplitude and phase distribution of the point spread function of the metasurface are obtained by numerical calculation.

focal plane of a 4F imaging system, spiral phase contrast and bright-field imaging mode can be controlled by the incident circular polarization states. However, this approach still cannot synchronously realize two imaging modes. In addition, it relies on a bulky 4F system and the incident light has to be in circular polarization.

In this work, we propose a compact dielectric metasurface that can simultaneously generate spiral phase contrast and bright-field imaging in the same field of view. Taking advantage of the flexible phase design of the metasurface, the spiral phase, parabolic phase, and deflection phase are superimposed on the same metasurface through selecting a series of rotationally symmetrical nanostructures. As a result, the entire imaging process can only rely on the single-layer metasurface without the requirements of a 4F system and incident polarization. We envision that the proposed compact and multifunctional metasurface may have great application potentials in the fields of biomedical imaging and materials science.[41,42]

A schematic illustration of synchronous spiral phase contrast imaging and bright-field imaging based on a single metasurface is shown in Figure 1a. After coherent light illuminates the object and is then modulated by the metasurface, two images, including a spiral phase contrast edge image and a bright-field entire image, appear at the imaging plane of the metasurface in the same field of view. The design principle and phase distribution of the metasurface are depicted in Figure 1b. To realize spiral phase contrast imaging, a spiral phase $\varphi_S = \theta$ with a topological charge of +1 is superimposed with the parabolic focusing phase $\varphi_P = -k_0 r^2/2f$ to generate the spiral lens phase, where θ and r are the azimuth and radial coordinates of the metasurface, respectively, k_0 is the free-space wavenumber, and $f = 1145\ \mu$m is the designed focal length. On the other side, for

https://doi.org/10.1021/acs.nanolett.3c00388
Nano Lett. 2023, 23, 2991−2997

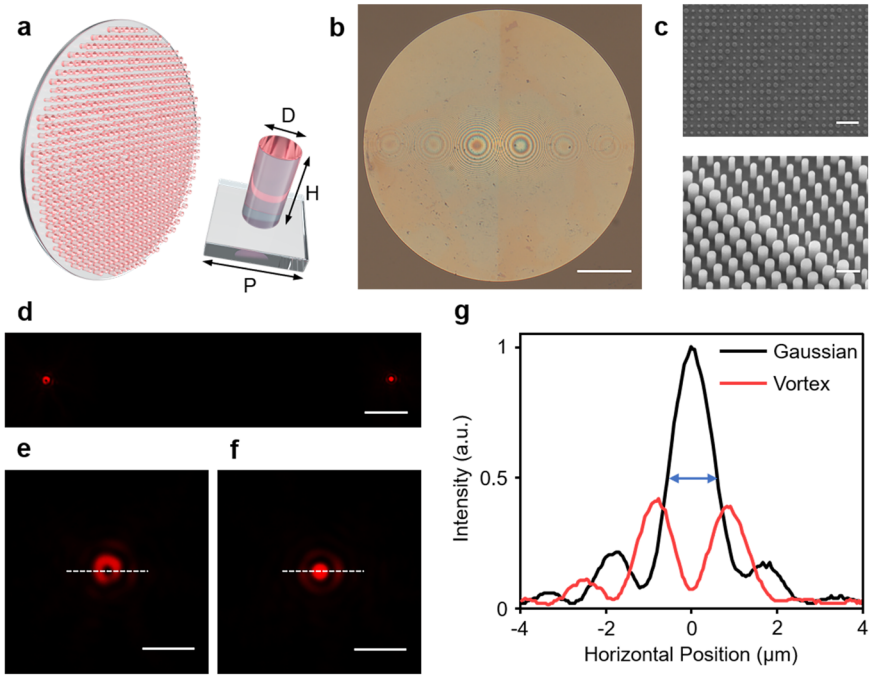

Figure 2. (a) Schematic diagram of the designed dielectric metasurface. Inset: perspective view of the unit cell. *D*, *H*, and *P* represent the diameter, height, and square lattice constant, respectively. (b) Optical photograph of the fabricated metasurface with a diameter of 1 mm. Scale bar: 200 μm. (c) Top and oblique views of the SEM images. Scale bars: 1 μm (top) and 500 nm (bottom). (d) Experimentally measured PSF_{meta} at a wavelength of 630 nm. Scale bar: 20 μm. (e, f) Magnified intensity distributions of the focal spots. Scale bar: 5 μm. (g) Horizontal cross-sectional normalized intensity curves along the dotted line. The fwhm of the Gaussian is 1.12 μm, and the distance between the two main peaks of the vortex is 1.60 μm.

realizing bright-field imaging, a constant phase φ_C is superimposed with the parabolic focusing phase φ_P to generate the focusing lens phase. To spatially separate the spiral phase contrast and bright-field images, a deflection phase $\varphi_D = k_0 sx/f$ is also introduced here, where the separation distance from the center is s = 80 μm. As a result, the final target phase distribution φ_{TP} of the metasurface can be obtained by $\varphi_{TP} = \arg\{\exp[i(\varphi_S + \varphi_P - \varphi_D)] + \exp[i(\varphi_C + \varphi_P + \varphi_D)]\}$.

In an ideal imaging system, the electric field of the coherent image $U_i(x_i,y_i)$ can be expressed as the convolution of the electric field of the object $U_o(x_o,y_o)$ and the point spread function (PSF_{meta}) of the system, following

$$U_i(x_i, y_i) = U_o(x_o, y_o) \otimes PSF_{meta} \quad (1)$$

Here PSF_{meta} is obtained by a numerical calculation using the angular spectrum method (ASM), and its amplitude and phase distributions are depicted in Figure 1c. As expected, the metasurface with phase distribution of φ_{TP} gives the system a donut-shaped and Gaussian intensity distribution. For the donut-shaped PSF_{meta} in the form of a vortex, the metasurface imparts an orbital angular momentum (OAM) with topological charge +1 to the incident light field and introduces a phase difference of π between the positive and negative spatial frequencies. According to eq 1, when the electric field of object U_o is convolved with donut-shaped PSF_{meta}, destructive interference occurs in the uniform region and leads to a dark background. In contrast, arbitrary unevenness including amplitude gradient and phase gradient in the region of integration will remove this destructive interference, which leads to a strong isotropic edge contrast enhancement of the observed object (see Note 1 in the Supporting Information for details). On the other side, similar to the conventional lens, the Gaussian PSF_{meta} interacts with U_o at the object plane will form a bright-field image.

Figure 2a indicates the schematic diagram of the proposed dielectric metasurface, which is formed by a series of isotropic silicon nanopillars with same height of 600 nm but different diameters. At the designed wavelength of 630 nm, the square lattice constant P of the nanopillars array is set to 300 nm to suppress higher order diffraction and satisfy the Nyquist−Shannon sampling theorem. In order to satisfy the full phase coverage of 0−2π, the nanopillar's diameter D is chosen as 16 discrete lengths ranging from 90 to 210 nm (see Note 2 in the Supporting Information for details). The isotropic nanopillars ensure that the optical field phase modulation is insensitive to the polarization state. Figure 2b,c shows the optical photograph and scanning electron microscope (SEM) images of the fabricated metasurface. The sample is fabricated from a 600 nm thick crystalline silicon film epitaxially grown on a transparent substrate. Through electron beam lithography (EBL) and inductively coupled plasma-reactive ion etching (ICP-RIE) technology, a metasurface sample with 1 mm diameter is obtained. The detailed fabrication process is described in Note 3 in the Supporting Information.

To evaluate the performance of the fabricated metasurface, the intensity distribution of the PSF is measured at the wavelength of 630 nm, as shown in Figure 2d. It can be clearly seen that a donut-shaped vortex beam is focused on the left side of the focal plane while a focal point with Gaussian intensity distribution appears on the right side of the focal plane. These results agree well with the calculations shown in Figure 1c. The intensity distribution along the x−z plane is given in Figure S3 in the Supporting Information. The center-to-center distance between the two focal spots is 160 μm, and the focal length is 1170 μm. Such a lateral separation distance

https://doi.org/10.1021/acs.nanolett.3c00388
Nano Lett. 2023, 23, 2991−2997

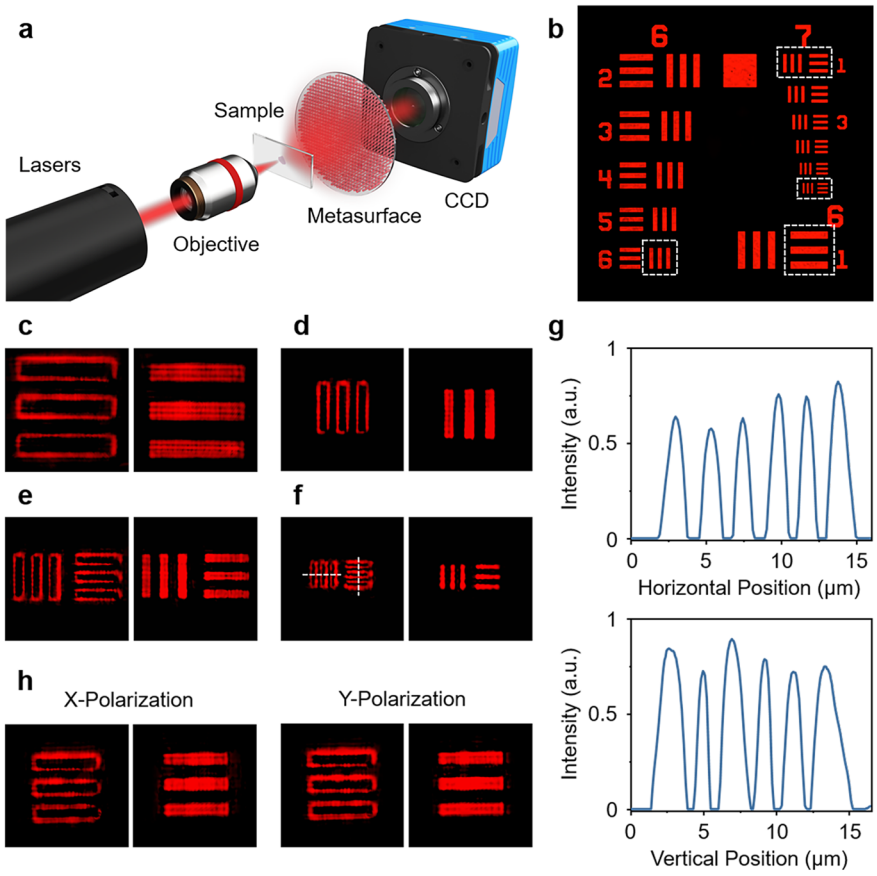

Figure 3. (a) Sketch of the experimental setup for simultaneous spiral phase contrast and bright-field imaging. (b) Optical photograph of the 1951 USAF resolution test chart. (c–f) Synchronously captured spiral phase contrast and bright-field images corresponding to the elements (6-1, 6-6, 7-1 and 7-6) in the dashed boxes in (b), respectively. (g) Horizontal and vertical cross-sectional normalized intensity curves of the spiral phase contrast image in the (f). (h) Spiral phase contrast and bright-field images of the element 6-4 illuminated with light in orthogonal *x* and *y* polarization states.

can well avoid off-axis aberrations in the imaging process and reduce crosstalk between the two images. Figure 2e,f shows the magnified images of two focal spots, respectively. The uniform donut and Gaussian intensity distributions indicate that the metasurface will simultaneously perform isotropic edge-enhanced imaging and bright-field imaging as expected. The horizontal cross-sectional normalized intensity curves obtained along the dotted line in the figure are shown in Figure 2g. The full width at half-maximum (fwhm) of the Gaussian PSF is 1.12 μm, and the distance between the two main peaks of the donut-shaped PSF is 1.60 μm, which agree with the theoretical values of 1.05 and 1.20 μm, respectively.

The imaging experimental setup of the metasurface for synchronous spiral phase contrast and bright-field imaging is sketched in Figure 3a. A supercontinuum laser modulated by an acousto-optic tunable filter (AOTF) system emits a 630 nm laser beam and focuses it on the observed object by a microscope objective with a 4× magnification and numerical aperture of 0.1. The transmitted light through the object is then modulated by the metasurface and captured by a charge-coupled-device (CCD) camera. Through reasonably adjusting the distance between the object and the image, magnified phase-contrast and bright-field images can be simultaneously obtained at the imaging plane. In order to evaluate the imaging performance of the system, we first use the 1951 United States Air Force (1951 USAF) resolution test chart as an observed object for an imaging experiment. Figure 3b is the optical photograph of groups 6 and 7 in the resolution test chart. Figure 3c–f shows the spiral phase contrast and bright-field images corresponding to the test targets 6-1, 6-6, 7-1, and 7-6 indicated by the white dashed lines in Figure 3b, respectively, which correspond to resolutions of 15.6, 8.8, 7.8, and 4.4 μm per line pair. These results imply that the proposed metasurface imaging system can well resolve the structure with a line width of 2.2 μm in spiral phase contrast and bright-field modes. The normalized intensity curves obtained along the horizontal and vertical dashed lines in the spiral phase contrast image of Figure 3f are given in Figure 3g. The uniform edge intensity distribution indicates that the system has a good isotropic edge enhancement. Figure 3h displays the results of spiral phase contrast and bright-field imaging (6-4 test target) for the incident light in *x* and *y* polarization states, respectively. These two sets of images are almost identical, which originates from the fact that unit cells of the metasurface are nanopillars with rotational symmetry.

Next, we use one amplitude object and one phase object to demonstrate the imaging experiment. Figure 4a shows spiral phase contrast and bright-field images with about 39.5× magnification of amplitude object "META" obtained simultaneously at the image plane of the metasurface with the illumination of a laser beam at a wavelength of 630 nm. Here, the microstructure patterns are fabricated by focused ion beam (FIB) milling on an opaque gold film. Obviously, the spiral phase contrast window on the left has eliminated the low-

https://doi.org/10.1021/acs.nanolett.3c00388
Nano Lett. 2023, 23, 2991−2997

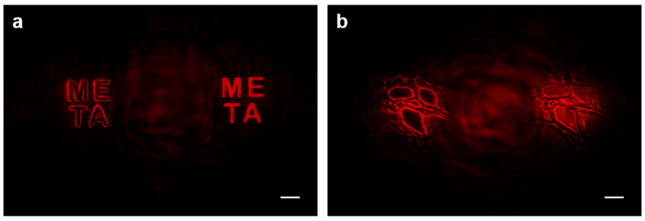

Figure 4. Synchronously captured spiral phase contrast and bright-field images in the same field of view. Experimental results obtained at the image plane for (a) the metallic mask patterned with characters of "META" and (b) unstained limewood stem cells as objects, respectively, at a wavelength of 630 nm. Scale bar: 20 μm.

frequency portion of the light field, delineating the edges of the microstructure patterns. The right bright-field effectively preserves the information within the cutoff frequency to show the full view of the patterns. Besides using an amplitude object, we also use unstained limewood stem cells as the phase object to verify the dual-mode imaging capability of the metasurface. As shown in Figure 4b, it is difficult to distinguish the boundaries between neighboring unstained cells in the bright-field window, while the outline of the cells is clearly revealed under the spiral phase contrast window. By collecting different frequency information on the same specimens in two windows at the same time, this will significantly improve the observation and identification of cell morphology. It is worth noting that there is a bright spot in the center due to the transmitted light from the weak zeroth-order diffraction. However, this bright spot is mainly concentrated in the center of the image plane and has a relatively small effect on the spiral phase contrast and bright-field images. In principle, to further reduce this effect, we can design an off-axis aberration-eliminating metasurface with large deflection angles by optimizing the phase distribution. This approach can increase the lateral distance between the two images, which will further minimize the impact of the bright spot on the images.

In addition to the designed wavelength, the metasurface can also work for the other visible wavelengths, benefiting from the similar phase difference tendency and full phase coverage of the selected nanopillars within the broad band. Figure 5a–c and Figure 5d–f show the spiral phase contrast and bright-field images of the amplitude object "META" and the phase object unstained limewood stem cells illuminated by the supercontinuum laser filtered at the wavelengths of 530, 580, and 680 nm, respectively. Due to the existence of the chromatic diffraction dispersion, for these three wavelengths, the corresponding focal lengths of the metasurface shift to 1385, 1281, and 1096 μm, respectively (see Note 5 in the Supporting Information for details). Moreover, the magnifications of the images gradually increase with the red shift of the illuminating wavelength, which are about 32.5×, 36.6× and 43.2×, respectively. In the visible wavelength range of 150 nm (from 530 to 680 nm), the spiral phase contrast and bright-field windows still well exhibit the edge and entire information on the observed objects. These results indicate that the metasurface-based imaging system has a broad-band response.

In conclusion, we propose and demonstrate a dielectric metasurface that synchronously performs edge-enhanced spiral phase contrast imaging and diffraction-limited bright-field imaging. The metasurface is formed of silicon nanopillars with

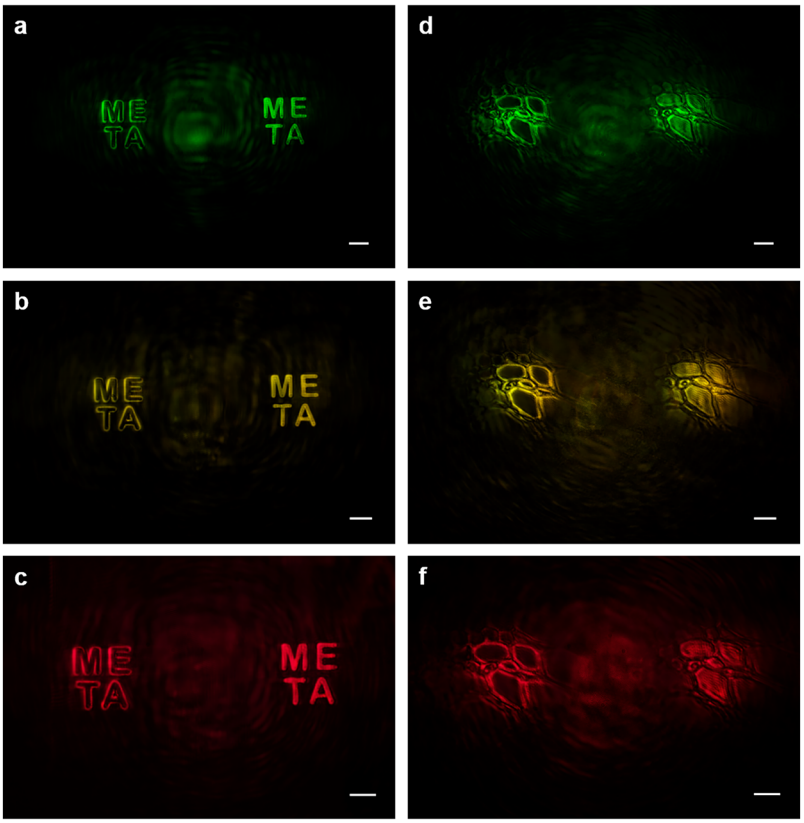

Figure 5. Simultaneously captured spiral phase contrast and bright-field images of (a–c) "META" mask and (d–f) unstained limewood stem cells at the image plane illuminated by a laser beam at wavelengths of 530, 580, and 680 nm, respectively. Scale bar: 20 μm.

https://doi.org/10.1021/acs.nanolett.3c00388
Nano Lett. 2023, 23, 2991–2997

rotational symmetry, which makes the imaging system insensitive to the incident polarization states. In experiments, amplitude objects of a patterned metallic mask and phase object of unstained transparent limewood stem cells are both used to verify the imaging functionalities of the metasurface system. Considering the advantages of planar architecture and ultrathin thickness of the metasurface, this approach is expected to have good application potentials in the fields of microscopy, biomedicine, and materials science.

■ ASSOCIATED CONTENT

Supporting Information

The Supporting Information is available free of charge at https://pubs.acs.org/doi/10.1021/acs.nanolett.3c00388.

Principle of spiral phase contrast imaging, complex refractive index of crystalline silicon, simulation of phase modulation in dielectric nanopillars, nanofabrication of the metasurface, intensity distributions of the focal spots along the $x-z$ plane, and the broad-band response of the metasurface in the visible region (PDF)

■ AUTHOR INFORMATION

Corresponding Author

Ting Xu − *National Laboratory of Solid-State Microstructures, Jiangsu Key Laboratory of Artificial Functional Materials, College of Engineering and Applied Sciences, Nanjing University, Nanjing 210093, People's Republic of China; Collaborative Innovation Center of Advanced Microstructures, Nanjing 210093, People's Republic of China;* orcid.org/0000-0002-0704-1089; Email: xuting@nju.edu.cn

Authors

Yanzeng Zhang − *National Laboratory of Solid-State Microstructures, Jiangsu Key Laboratory of Artificial Functional Materials, College of Engineering and Applied Sciences, Nanjing University, Nanjing 210093, People's Republic of China*

Peicheng Lin − *National Laboratory of Solid-State Microstructures, Jiangsu Key Laboratory of Artificial Functional Materials, College of Engineering and Applied Sciences, Nanjing University, Nanjing 210093, People's Republic of China*

Pengcheng Huo − *National Laboratory of Solid-State Microstructures, Jiangsu Key Laboratory of Artificial Functional Materials, College of Engineering and Applied Sciences, Nanjing University, Nanjing 210093, People's Republic of China; Collaborative Innovation Center of Advanced Microstructures, Nanjing 210093, People's Republic of China*

Mingze Liu − *National Laboratory of Solid-State Microstructures, Jiangsu Key Laboratory of Artificial Functional Materials, College of Engineering and Applied Sciences, Nanjing University, Nanjing 210093, People's Republic of China*

Yongze Ren − *National Laboratory of Solid-State Microstructures, Jiangsu Key Laboratory of Artificial Functional Materials, College of Engineering and Applied Sciences, Nanjing University, Nanjing 210093, People's Republic of China*

Song Zhang − *National Laboratory of Solid-State Microstructures, Jiangsu Key Laboratory of Artificial Functional Materials, College of Engineering and Applied Sciences, Nanjing University, Nanjing 210093, People's Republic of China*

Qianwei Zhou − *National Laboratory of Solid-State Microstructures, Jiangsu Key Laboratory of Artificial Functional Materials, College of Engineering and Applied Sciences, Nanjing University, Nanjing 210093, People's Republic of China*

Yilin Wang − *National Laboratory of Solid-State Microstructures, Jiangsu Key Laboratory of Artificial Functional Materials, College of Engineering and Applied Sciences, Nanjing University, Nanjing 210093, People's Republic of China*

Yan-qing Lu − *National Laboratory of Solid-State Microstructures, Jiangsu Key Laboratory of Artificial Functional Materials, College of Engineering and Applied Sciences, Nanjing University, Nanjing 210093, People's Republic of China; Collaborative Innovation Center of Advanced Microstructures, Nanjing 210093, People's Republic of China;* orcid.org/0000-0001-6151-8557

Complete contact information is available at: https://pubs.acs.org/10.1021/acs.nanolett.3c00388

Author Contributions

Y.Z., P.L., P.H., and M.L. carried out the theoretical design, numerical simulations, and experimental measurements. All authors contributed toward the interpretation of results and participated in manuscript preparation. T.X. directed the project.

Notes

The authors declare no competing financial interest.

■ ACKNOWLEDGMENTS

This work was supported in part by the National Natural Science Foundation of China (12274217), the Natural Science Foundation of Jiangsu Province (BK20220068 and BK20212004), and the Fundamental Research Funds for Central Universities.

■ REFERENCES

(1) Park, Y.; Depeursinge, C.; Popescu, G. Quantitative phase imaging in biomedicine. *Nature Photon* **2018**, *12*, 578−589.

(2) Zernike, F. How I discovered phase contrast. *Science* **1955**, *121*, 345−349.

(3) Preza, C.; Snyder, D. L.; Conchello, J. A. Theoretical development and experimental evaluation of imaging models for differential-interference-contrast microscopy. *J. Opt. Soc. Am. A* **1999**, *16*, 2185−2199.

(4) Davis, J. A.; McNamara, D. E.; Cottrell, D. M.; et al. Image processing with the radial Hilbert transform: theory and experiments. *Opt. Lett.* **2000**, *25*, 99−101.

(5) Guo, C.; Han, Y.; Xu, J.; et al. Radial Hilbert transform with Laguerre-Gaussian spatial filters. *Opt. Lett.* **2006**, *31*, 1394−1396.

(6) Ritsch-Marte, M. Orbital angular momentum light in microscopy. *Philos. Trans. R. Soc. A* **2017**, *375*, 20150437.

(7) Maurer, C.; Jesacher, A.; Bernet, S.; et al. What spatial light modulators can do for optical microscopy. *Laser Photonics Rev.* **2011**, *5*, 81−101.

(8) Kwon, H.; Arbabi, E.; Kamali, S. M.; et al. Single-shot quantitative phase gradient microscopy using a system of multifunctional metasurfaces. *Nature Photon* **2020**, *14*, 109−114.

(9) Zhao, M.; Liang, X.; Li, J.; et al. Optical phase contrast microscopy with incoherent vortex phase. *Laser Photonics Rev.* **2022**, *16*, 2200230.

(10) Jesacher, A.; Furhapter, S.; Bernet, S.; et al. Shadow effects in spiral phase contrast microscopy. *Phys. Rev. Lett.* **2005**, *94*, 233902.
(11) Furhapter, S.; Jesacher, A.; Bernet, S.; et al. Spiral phase contrast imaging in microscopy. *Opt. Express* **2005**, *13*, 689−694.
(12) Bernet, S.; Jesacher, A.; Fürhapter, S.; et al. Quantitative imaging of complex samples by spiral phase contrast microscopy. *Opt. Express* **2006**, *14*, 3792−3805.
(13) Situ, G.; Pedrini, G.; Osten, W. Spiral phase filtering and orientation-selective edge detection/enhancement. *J. Opt. Soc. Am. A* **2009**, *26*, 1788−1797.
(14) Kim, T.; Zhou, R.; Mir, M.; et al. White-light diffraction tomography of unlabelled live cells. *Nature Photon* **2014**, *8*, 256−263.
(15) Wang, J.; Zhang, W.; Qi, Q.; et al. Gradual edge enhancement in spiral phase contrast imaging with fractional vortex filters. *Sci. Rep* **2015**, *5*, 15826.
(16) Yu, N.; Capasso, F. Flat optics with designer metasurfaces. *Nat. Mater.* **2014**, *13*, 139−150.
(17) Arbabi, A.; Horie, Y.; Bagheri, M.; et al. Dielectric metasurfaces for complete control of phase and polarization with subwavelength spatial resolution and high transmission. *Nat. Nanotechnol.* **2015**, *10*, 937−943.
(18) Pahlevaninezhad, M.; Huang, Y. W.; Pahlevani, M.; et al. Metasurface-based bijective illumination collection imaging provides high-resolution tomography in three dimensions. *Nature Photon* **2022**, *16*, 203−211.
(19) Guo, Y.; Zhang, S.; Pu, M.; et al. Spin-decoupled metasurface for simultaneous detection of spin and orbital angular momenta via momentum transformation. *Light Sci. Appl.* **2021**, *10*, 63.
(20) Kim, Y.; Lee, G. Y.; Sung, J.; et al. Spiral metalens for phase contrast imaging. *Adv. Funct. Mater.* **2022**, *32*, 2106050.
(21) Zhang, F.; Pu, M.; Li, X.; et al. All-dielectric metasurfaces for simultaneous giant circular asymmetric transmission and wavefront shaping based on asymmetric photonic spin-orbit interactions. *Adv. Funct. Mater.* **2017**, *27*, 1704295.
(22) Liu, M.; Zhu, W.; Huo, P.; et al. Multifunctional metasurfaces enabled by simultaneous and independent control of phase and amplitude for orthogonal polarization states. *Light Sci. Appl.* **2021**, *10*, 107.
(23) Zhou, Y.; Zheng, H.; Kravchenko, I. I.; et al. Flat optics for image differentiation. *Nature Photon* **2020**, *14*, 316−323.
(24) Schlickriede, C.; Kruk, S.; Wang, L.; et al. Nonlinear imaging with all-dielectric metasurfaces. *Nano Lett.* **2020**, *20*, 4370−4376.
(25) Wen, D.; Cadusch, J.; Meng, J.; et al. Vectorial holograms with spatially continuous polarization distributions. *Nano Lett.* **2021**, *21*, 1735−1741.
(26) Zhou, J.; Wu, Q.; Zhao, J.; et al. Fourier Optical Spin Splitting Microscopy. *Phys. Rev. Lett.* **2022**, *129*, No. 020801.
(27) Liang, H.; Lin, Q.; Xie, X.; et al. Ultrahigh numerical aperture metalens at visible wavelengths. *Nano Lett.* **2018**, *18*, 4460−4466.
(28) Luo, Y.; Chu, C.; Vyas, S.; et al. Varifocal metalens for optical sectioning fluorescence microscopy. *Nano Lett.* **2021**, *21*, 5133−5142.
(29) Ren, H.; Fang, X.; Jang, J.; et al. Complex-amplitude metasurface-based orbital angular momentum holography in momentum space. *Nat. Nanotechnol.* **2020**, *15*, 948−955.
(30) Deng, Z.; Jin, M.; Ye, X.; et al. Full-color complex-amplitude vectorial holograms based on multi-freedom metasurfaces. *Adv. Funct. Mater.* **2020**, *30*, 1910610.
(31) Meng, W.; Hua, Y.; Cheng, K.; et al. 100 Hertz frame-rate switching three-dimensional orbital angular momentum multiplexing holography via cross convolution. *Opto-Electron Sci.* **2022**, *1*, 220004.
(32) Huo, P.; Song, M.; Zhu, W.; et al. Photorealistic full-color nanopainting enabled by a low-loss metasurface. *Optica* **2020**, *7*, 1171−1172.
(33) Song, M.; Feng, L.; Huo, P.; et al. Versatile full-colour nanopainting enabled by a pixelated plasmonic metasurface. *Nat. Nanotechnol.* **2023**, *18*, 71−78.
(34) Fu, R.; Chen, K.; Li, Z.; et al. Metasurface-based nanoprinting: principle, design and advances. *Opto-Electron Sci.* **2022**, *1*, 220011.
(35) Xiong, J.; Cai, X.; Cui, K.; et al. Dynamic brain spectrum acquired by a real-time ultraspectral imaging chip with reconfigurable metasurfaces. *Optica* **2022**, *9*, 461−468.
(36) Cordaro, A.; Kwon, H.; Sounas, D.; et al. High-index dielectric metasurfaces performing mathematical operations. *Nano Lett.* **2019**, *19*, 8418−8423.
(37) Fu, W.; Zhao, D.; Li, Z.; et al. Ultracompact meta-imagers for arbitrary all-optical convolution. *Light Sci. Appl.* **2022**, *11*, 62.
(38) Xu, D.; Yang, H.; Xu, W.; et al. Inverse design of Pancharatnam-Berry phase metasurfaces for all-optical image edge detection. *Appl. Phys. Lett.* **2022**, *120*, 241101.
(39) Wang, Z.; Hu, G.; Wang, X.; et al. Single-layer spatial analog meta-processor for imaging processing. *Nature Commun.* **2022**, *13*, 2188.
(40) Huo, P.; Zhang, C.; Zhu, W.; et al. Photonic spin-multiplexing metasurface for switchable spiral phase contrast imaging. *Nano Lett.* **2020**, *20*, 2791−2798.
(41) Qian, J.; Cao, Y.; Bi, Y.; et al. Structured illumination microscopy based on principal component analysis. *eLight* **2023**, *3*, 4.
(42) Sadraeian, M.; Zhang, L.; Aavani, F.; et al. Viral inactivation by light. *eLight* **2022**, *2*, 18.

https://doi.org/10.1021/acs.nanolett.3c00388
Nano Lett. 2023, 23, 2991−2997